**PAPER**

# High-pressure structural and vibrational properties of monazite-type BiPO$_4$, LaPO$_4$, CePO$_4$, and PrPO$_4$

View the article online for updates and enhancements.

# High-pressure structural and vibrational properties of monazite-type BiPO$_4$, LaPO$_4$, CePO$_4$, and PrPO$_4$

D Errandonea[1], O Gomis[2], P Rodríguez-Hernández[3], A Muñoz[3],
J Ruiz-Fuertes[1,8], M Gupta[1], S N Achary[4], A Hirsch[5], F J Manjon[6],
L Peters[5], G Roth[5], A K Tyagi[4] and M Bettinelli[7]

[1] Departamento de Física Aplicada-ICMUV, MALTA Consolider Team, Universitat de València,
Edificio de Investigación, C/Dr. Moliner 50, Burjassot, 46100 Valencia, Spain
[2] Centro de Tecnologías Físicas, MALTA Consolider Team, Universitat Politècnica de València, 46022
Valencia, Spain
[3] Departamento de Física, Instituto de Materiales y Nanotecnología, MALTA Consolider Team,
Universidad de La Laguna, La Laguna, 38205 Tenerife, Spain
[4] Chemistry Division, Bhabha Atomic Research Centre, Mumbai 400085, India
[5] Institut für Kristallographie, RWTH Aachen University, Jägerstraße 17-19, 52066 Aachen, Germany
[6] Instituto de Diseño para la Fabricación y Producción Automatizada, MALTA Consolider Team,
Universitat Politècnica de València, 46022 Valencia, Spain
[7] Luminescent Materials Laboratory, DB and INSTM, Università di Verona, Strada Le Grazie 15, 37134
Verona, Italy

E-mail: daniel.errandonea@uv.es

CrossMark

## Abstract

Monazite-type BiPO$_4$, LaPO$_4$, CePO$_4$, and PrPO$_4$ have been studied under high pressure by
*ab initio* simulations and Raman spectroscopy measurements in the pressure range of stability
of the monazite structure. A good agreement between experimental and theoretical Raman-
active mode frequencies and pressure coefficients has been found which has allowed us to
discuss the nature of the Raman-active modes. Besides, calculations have provided us with
information on how the crystal structure is modified by pressure. This information has allowed
us to determine the equation of state and the isothermal compressibility tensor of the four
studied compounds. In addition, the information obtained on the polyhedral compressibility
has been used to explain the anisotropic axial compressibility and the bulk compressibility of
monazite phosphates. Finally, we have carried out a systematic discussion on the high-pressure
behavior of the four studied phosphates in comparison to results of previous studies.

Keywords: monazite, orthophosphate, high pressure, equation of state, Raman,
*Ab initio* calculations

(Some figures may appear in colour only in the online journal)

[8] Current address: Department of Earth Sciences and Condensed Matter
Physics, University of Cantabria, Santander, Spain.

## 1. Introduction

Monazite is a widespread phosphate mineral containing rare-earth metals [1] that can be found as an accessory component in granites and carbonatites, as well as in volcanic and metamorphic rocks. The crystal structure of monazite is monoclinic, belonging to space group $P2_1/n$ [1]. A schematic view of the crystal structure is shown in figure 1. It can be seen as an alternating chain of phosphorus-oxygen $PO_4$ tetrahedra and trivalent cation-oxygen $AO_9$ polyhedra. In addition to the mineralogical interest, monazite has also called the attention of scientists due to a plethora of potential technological applications, like nuclear waste management, catalysis and optical devices [2, 3].

The knowledge obtained from high-pressure (HP) research is of interest for the applications of monazites [3]. In this context, several HP studies have been published on monazite-type phosphates after the seminal work carried out by Lacomba-Perales *et al* at the beginning of this decade [4]. In particular, it has been found that a pressure-induced phase transition occurs in monazite-type $LaPO_4$ at a pressure higher than $26\,GPa$ and that the maximum pressure of stability of the monazite phase is shifted towards higher pressures as the size of the trivalent cation is reduced [4, 5].

It must be noted that previous HP studies on monazites have not only focused on the occurrence of pressure-induced phase transitions [4–6], but also on the crystal chemistry of rare-earth phosphates under compression [7], on their mechanical behavior [8], on the structural response to pressure [9], and on the elastic properties [10]. In spite of all these efforts, a systematic understanding of the structural behavior and compressibility of monazite-type oxides has not been achieved yet. In addition to this, an unusual structural distortion has been reported in $CePO_4$ at $11.5\,GPa$, a pressure much lower than the expected transition pressure ($>30\,GPa$) [11]. The reasons for this observation remained unclear.

The collection of HP studies above summarized reveal that additional research is needed with the aim of improving the knowledge of properties for this group of phosphates. For instance, the behavior of the Raman-active modes of monazites under compression has been studied only for $CePO_4$ up to $12\,GPa$ [11] and for $LaPO_4$ microspheres and hollow spheres up to $28\,GPa$ [12, 13]. Therefore, in this work we report a joint experimental and theoretical vibrational study on several monazites: bismuth phosphate ($BiPO_4$), lanthanum phosphate ($LaPO_4$), cerium phosphate ($CePO_4$), and praseodymium phosphate ($PrPO_4$). We have scrutinized the HP behavior of the vibrational properties of these compounds by means of *ab initio* calculations and Raman spectroscopy measurements up to pressures between 24 and $32\,GPa$; i.e. only in the region of stability of the monazite phase of the different samples. A similar approach has been recently proven to be quite efficient in order to study related compounds under HP conditions [14–16]. The study of pressure-induced phase transitions in these monazite-type compounds is beyond the scope of this work.

## 2. Details of calculations

The influence of pressure on the crystal structure and Raman-active modes of monazite-type $BiPO_4$, $LaPO_4$, $CePO_4$, and $PrPO_4$ has been studied by *ab initio* calculations. The calculations were based on the density-functional theory (DFT) [17]. To implement them we employed the Vienna *ab initio* simulation package (VASP) [18] and pseudo-potentials with the projector-augmented wave scheme (PAW) [19]. In order to achieve accurate results, the set of plane waves was extended up to a $520\,eV$ cutoff energy and the exchange-correlation energy was expressed using the generalized-gradient approximation (GGA) with the Perdew–Burke–Ernzerhof for solid (PBEsol) functionals [20]. A dense grid of Monkhorst–Pack [21] k-special points was utilized for integrations in the Brillouin zone (BZ) achieving a convergence of 1 meV per formula unit in the total energy. All the structural parameters for the four studied monazites were optimized by minimizing, at selected volumes, the forces on the atoms and the stress tensor. This method has been successfully applied to study non-metallic oxides under pressure [22]. Phonon calculations were performed using the supercell method [23]. In all the calculations, we neglect the spin–orbit interaction following the conclusions of Blanca-Romero *et al* [24].

## 3. Experimental details

Single crystals of $LaPO_4$ and $PrPO_4$ were prepared by the flux method [25] using 99.99% purity reagents as presented in [5] and [26]. High-purity powders of $BiPO_4$ and $CePO_4$ were produced by precipitation from an aqueous solution and subsequent high-temperature treatments [25]. The crystal structure of all the prepared samples was confirmed to be monazite-type (monoclinic space group $P2_1/n$) by powder x-ray diffraction (XRD) using a Panalytical X-Pert system and Cu $K_\alpha$ radiation. These measurements indicated that the four phosphates were homogeneous and single phase materials with unit-cell parameters that within uncertainties agree with those reported in the literature [1, 27].

The Raman experiment on $LaPO_4$ was performed in quasi-backscattering configuration with a Renishaw (RM-1000) spectrometer. The excitation source was a Nd:YAG laser ($\lambda = 532\,nm$). Raman measurements in $BiPO_4$ and $CePO_4$ ($PrPO_4$) were carried out with a Horiba Jobin Yvon LabRAM HR UV (Jobin Yvon THR 1000) spectrometer using a He–Ne laser ($\lambda = 632.8\,nm$). In all set-ups, an edge filter was used to block the laser line. The incident power on the sample was 10 mW. The spectral resolution was better than $2\,cm^{-1}$.

HP experiments were carried out with different diamond-anvil cells (DACs) with diamond-culets of $300–350\,\mu m$. Samples were loaded in a $100\,\mu m$ hole of an Inconel or tungsten gasket pre-indented to a thickness of $40\,\mu m$. The ruby pressure standard was used for pressure determination [28, 29]. A 16:3:1 methanol-ethanol-water mixture was used as pressure-transmitting medium. During the DACs' loading, special attention was paid to occupy only a minor fraction on the pressure chamber with sample and
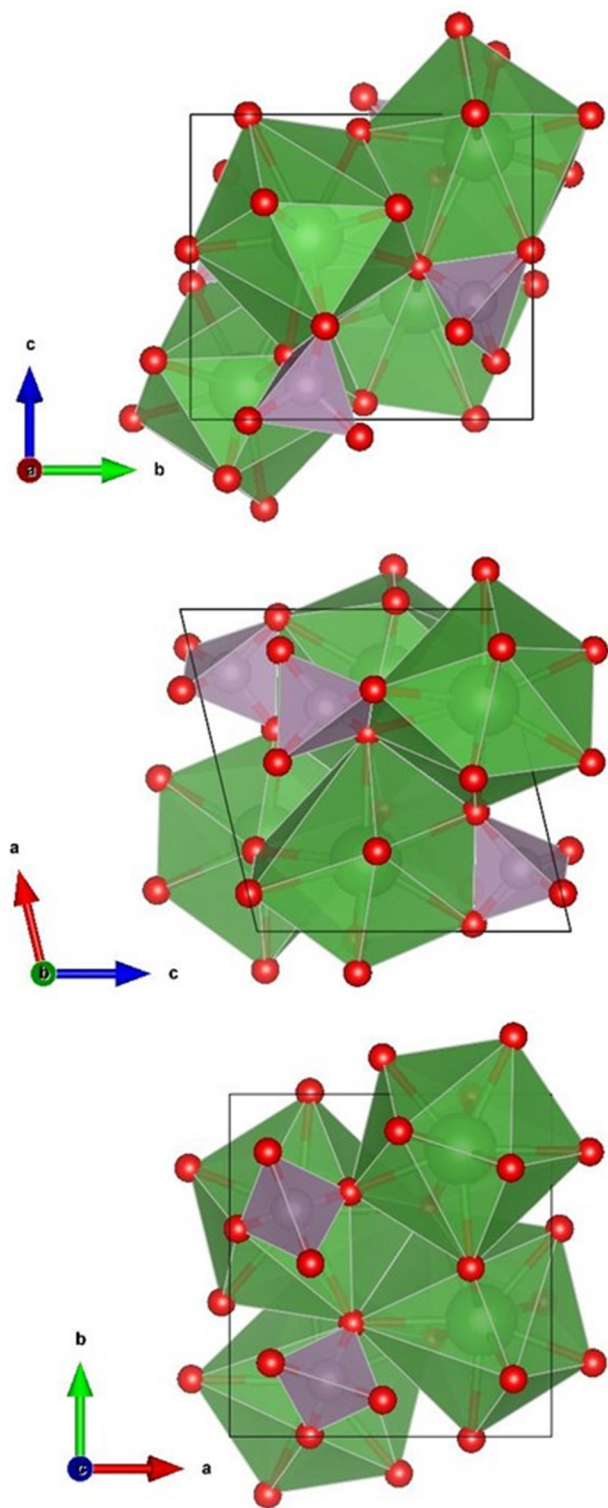
**Figure 1.** Three different views of the crystal structure of monazite-type orthophosphates. The PO$_4$ tetrahedral units and $A$O$_9$ polyhedral units are shown. Oxygen, phosphorus, and trivalent atoms are shown in red, purple, and green, respectively.

**Table 1.** Calculated structural parameters of monazite-type phosphates at ambient pressure.

BiPO$_4$, $a = 6.7549$ Å, $b = 6.9551$ Å, $c = 6.4700$ Å, $\beta = 103.95°$

| Atom | Site | $x$ | $y$ | $z$ |
|------|------|--------|--------|--------|
| Bi | 4e | 0.28394 | 0.14513 | 0.08817 |
| P | 4e | 0.29933 | 0.16215 | 0.61291 |
| O$_1$ | 4e | 0.25990 | 0.00537 | 0.44010 |
| O$_2$ | 4e | 0.37939 | 0.34210 | 0.51574 |
| O$_3$ | 4e | 0.46480 | 0.10182 | 0.81782 |
| O$_4$ | 4e | 0.11546 | 0.20505 | 0.70932 |

LaPO$_4$, $a = 6.8287$ Å, $b = 7.0579$ Å, $c = 6.4685$ Å, $\beta = 103.48°$

| Atom | Site | $x$ | $y$ | $z$ |
|------|------|--------|--------|--------|
| La | 4e | 0.28265 | 0.15941 | 0.10116 |
| P | 4e | 0.30465 | 0.16364 | 0.61258 |
| O$_1$ | 4e | 0.24907 | 0.00596 | 0.44319 |
| O$_2$ | 4e | 0.38162 | 0.33184 | 0.49641 |
| O$_3$ | 4e | 0.47491 | 0.10709 | 0.80619 |
| O$_4$ | 4e | 0.12746 | 0.21522 | 0.71180 |

CePO$_4$, $a = 6.8233$ Å, $b = 7.0520$ Å, $c = 6.4576$ Å, $\beta = 103.47°$

| Atom | Site | $x$ | $y$ | $z$ |
|------|------|--------|--------|--------|
| Ce | 4e | 0.28207 | 0.15864 | 0.10059 |
| P | 4e | 0.30377 | 0.16289 | 0.61239 |
| O$_1$ | 4e | 0.24895 | 0.00545 | 0.44238 |
| O$_2$ | 4e | 0.38121 | 0.33146 | 0.49633 |
| O$_3$ | 4e | 0.47376 | 0.10652 | 0.80677 |
| O$_4$ | 4e | 0.12635 | 0.21407 | 0.71158 |

PrPO$_4$, $a = 6.7818$ Å, $b = 6.9999$ Å, $c = 6.4150$ Å, $\beta = 103.59°$

| Atom | Site | $x$ | $y$ | $z$ |
|------|------|--------|--------|--------|
| Pr | 4e | 0.28227 | 0.15795 | 0.10049 |
| P | 4e | 0.30335 | 0.16269 | 0.61286 |
| O$_1$ | 4e | 0.24896 | 0.00455 | 0.44089 |
| O$_2$ | 4e | 0.38163 | 0.33273 | 0.49717 |
| O$_3$ | 4e | 0.47385 | 0.10564 | 0.80926 |
| O$_4$ | 4e | 0.12492 | 0.21340 | 0.71290 |

carried out up to 24.7, 29.2, 28.7, and 31.2 GPa for LaPO$_4$, CePO$_4$, PrPO$_4$, and BiPO$_4$, respectively. The limitation in pressure in the LaPO$_4$ experiment was due to the occurring phase transition at 26 GPa [5].

## 4. Results and discussion

### 4.1. Crystal structure calculations

The calculated ambient pressure structural parameters of the four different monazite-type phosphates are given in table 1. The calculated structures show a close agreement with the experimental results [1, 27]. In our simulations, the deviation of the computed structural parameters from measurements is smaller ($<$1%) than in previous calculations [20, 24, 32–34].

From calculations, we obtained the pressure dependence of the unit-cell parameters and atomic coordinates. In the case of BiPO$_4$, the calculations have been already compared

ruby, minimizing the chance of sample bridging between the diamond anvils [30]. In the pressure range covered by the experiments, no substantial broadening or changes in the splitting of the ruby lines were observed, indicating that deviatoric stresses were small [31]. Experiments were
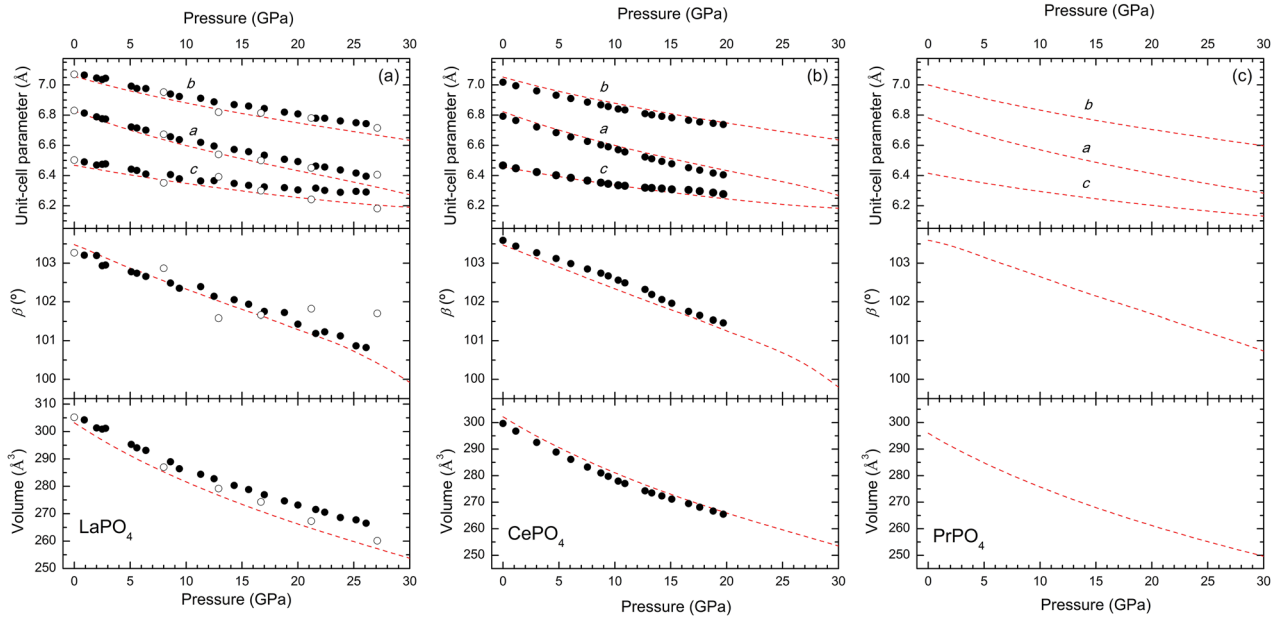
**Figure 2.** (Top) Pressure dependence of the lattice parameters. (Center) Pressure dependence of the $\beta$ angle. (Bottom) Pressure dependence of the unit-cell volume. (a) LaPO$_4$, (b) CePO$_4$, and (c) PrPO$_4$. Dashed lines represent the results of the calculations. For CePO$_4$, symbols are from powder XRD experiments [11]. For LaPO$_4$, empty symbols are from single-crystal XRD experiments [5] and solid symbols from powder XRD experiments [4].

with HP experiments [6], showing an excellent agreement in the pressure range covered by this study. Therefore, we will concentrate here in discussing the other three compounds. The results obtained for the unit-cell parameters of LaPO$_4$, CePO$_4$, and PrPO$_4$ are summarized in figure 2. For the first of the three compounds, the agreement with a single crystal XRD experiment [5] is very good; see figure 2(a). In contrast, the experimental results from a powder XRD experiment [4] deviate from calculations and the other experiment above 15 GPa, leading to a smaller compressibility. This deviation has been explained in the past as a consequence of inter-grain contact in powder experiments [5]. We also found similar deviations between powder XRD experiments [11] and theory for CePO$_4$; see figure 2(b). In this case, the effect is amplified, showing experiments a discontinuity in the slope of the pressure dependence of unit-cell parameters around 10 GPa. This phenomenon was attributed in the past to a pressure-induced structural distortion [11]. However, the results on LaPO$_4$ and the lack of structural distortions for any of the studied phosphates in our calculations suggest that the experimental results on CePO$_4$ can be affected by inter-grain contact and non-hydrostatic conditions [35]. In the case of PrPO$_4$, there are no experimental results to compare with. The results shown in figure 2(c) indicate that it has a behavior qualitatively similar to the other three phosphates.

From the present results and our previous study on BiPO$_4$ [6], it can be concluded that in monazite-type phosphates the compression is not isotropic as can be seen in the top panels of figure 2. In particular, the *a*-axis is the most compressible one and the *c*-axis the least compressible one. As a consequence, there is a tendency in the different compounds for the unit-cell parameter *a* to approach the value of *c*. On the other hand, in the central panels of figure 2, it can be seen that the monoclinic $\beta$ angle decreases under compression. In summary, all

**Table 2.** Third-order BM EOS determined for the studied compounds from theoretical calculations. The volume ($V_0$), bulk modulus ($B_0$), its pressure derivative ($B_0'$), and the implied value of the second pressure derivative ($B_0''$) are given.

| | $V_0$ (Å$^3$) | $B_0$ (GPa) | $B_0'$ (dimensionless) | $B_0''$ (GPa$^{-1}$) |
|---|---|---|---|---|
| LaPO$_4$ | 303.13(3) | 114.2(5) | 4.64(6) | −0.0432 |
| CePO$_4$ | 302.14(2) | 117.3(3) | 4.54(3) | −0.0402 |
| PrPO$_4$ | 295.91(4) | 120.2(6) | 4.59(7) | −0.0402 |
| BiPO$_4$ | 294.97(3) | 111.9(4) | 4.78(5) | −0.0472 |

these results indicate that there is a gradual symmetrization of the monazite structure under compression.

It might be noted that the behavior of monazite-type phosphates under compression is qualitatively similar to that found in other monazite-type oxides [15, 36]. Interestingly, we would like to insist here that no anomalous changes on the pressure dependence of the unit-cell parameters take place in any of the four studied phosphates or in other monazite-type oxides. Therefore, the kink previously found for the *c*-axis and $\beta$ angle at 11.5 GPa [11] appears to be an artifact caused by non-hydrostatic conditions.

From the theoretical pressure dependence of the unit-cell parameters, we determined the pressure dependence of the unit-cell volume (bottom panels of figure 2), which allowed us to obtain the theoretical room-temperature pressure-volume (P-V) equations of state (EOS). The results can be well described by a third-order Birch–Murnaghan (BM) EOS, whose parameters are summarized in table 2. For completeness, we also include in the table the implied second pressure-derivative of the bulk modulus [37]. The agreement between theory and previous experiments is good. For LaPO$_4$, calculations underestimate the bulk modulus ($B_0$) by 8 %
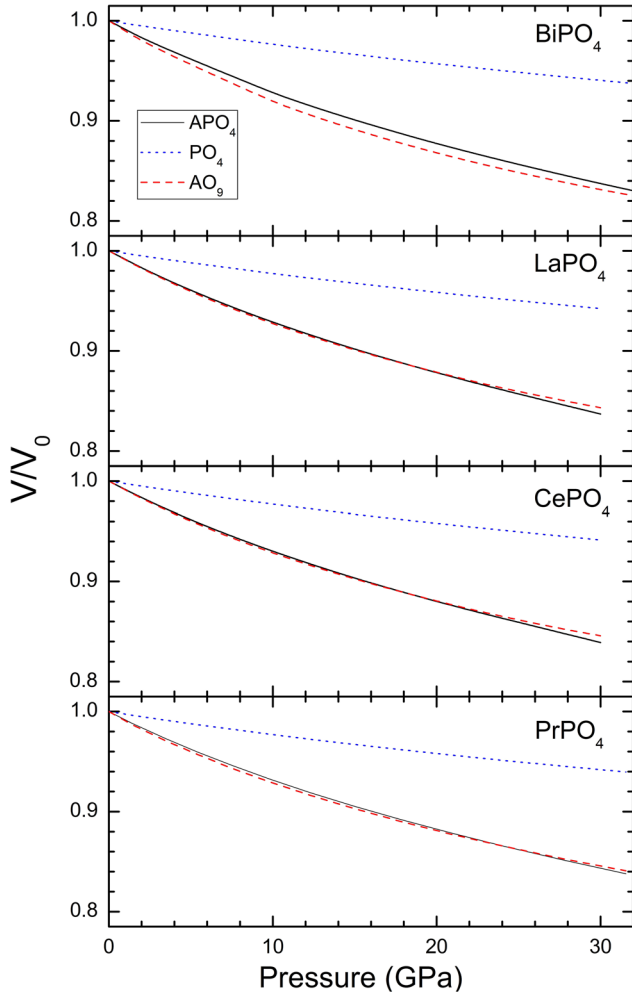
**Figure 3.** Relative variation with pressure of the unit-cell and polyhedral volume for the four studied compounds.



**Figure 4.** Distortion index of the $PO_4$ tetrahedron and $AO_9$ polyhedron as a function of pressure for the four studied compounds.

(in experiments $B_0 = 125$ GPa [5]). For $CePO_4$ calculations overestimate $B_0$ by 7% (in experiments $B_0 = 109$ GPa [11]). For $BiPO_4$ calculations underestimate $B_0$ by 5 % (in experiments $B_0 = 117$ GPa [6]). Therefore, for $PrPO_4$, which has never been studied experimentally under compression, we consider that $B_0 = 120$ GPa can be considered as an accurate estimation. On the other hand, our results suggest that from the previous $B_0$ values reported for $GdPO_4$, the most realistic is the one reported by Heffernan *et al* ($B_0 = 128$ GPa) [9]. There are three facts that deserve to be commented on table 2. The first is that monazite phosphates have a bulk modulus slightly larger than monazite-type vanadates ($B_0 = 95(5)$ GPa in $LaVO_4$ [15]) and are quite uncompressible in comparison with monazite-type chromates and selenates, which have $50$ GPa $< B_0 < 70$ GPa [38]. The second one is that monazite-type phosphates have a smaller bulk modulus than zircon-type phosphates [14] (e.g. $B_0 = 152(3)$ GPa in $HoPO_4$ and $B_0 = 144(3)$ in $TmPO_4$), which is a consequence of the larger unit-cell volume of monazite and the larger flexibility of the $AO_9$ polyhedron of monazite than the $AO_8$ polyhedron of zircon to distort in order to facilitate the volume contraction under compression (see figure 3). The third one is that the bulk modulus of the three rare-earth compounds $LaPO_4$,
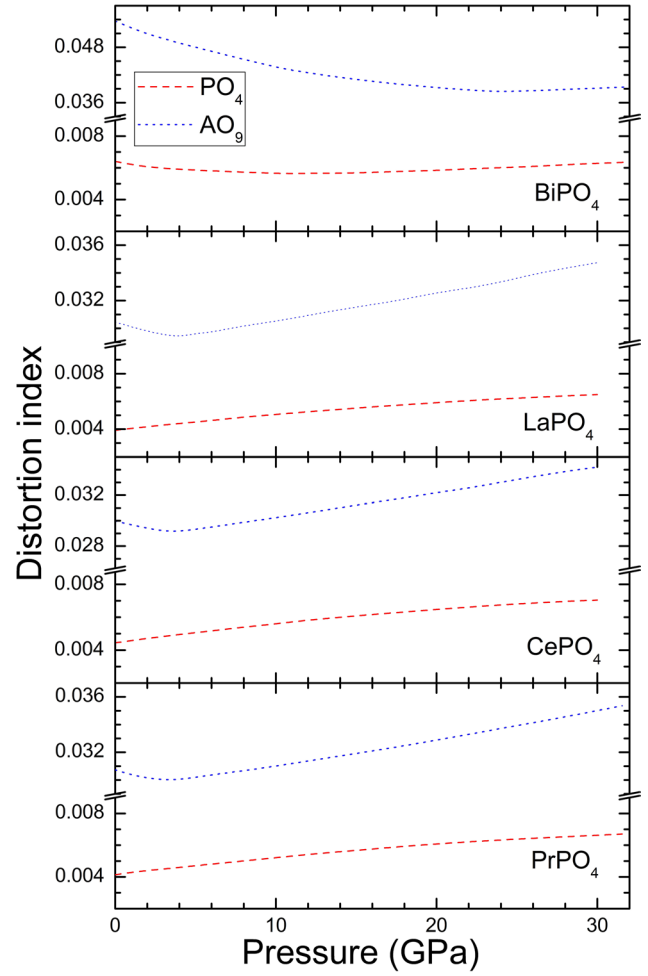
$CePO_4$, and $PrPO_4$ can be inversely correlated with the unit-cell volume at ambient pressure ($V_0$); see table 2. This is consistent with geometrical considerations which support that for similar oxide compounds one can expect that the product $B_0 \times V_0$ should be approximately constant [39]. Indeed, for these three phosphates the product is $35\,100 \pm 500$ Å$^3$ GPa. However, $BiPO_4$ does not follow this back-of-the-envelope rule. This compound has the smallest unit-cell volume and the smallest bulk modulus among the studied compounds being $B_0 \times V_0 \approx 33\,000$ Å$^3$ GPa. This distinctive behavior of $BiPO_4$ is a direct result of the presence of more compressible Bi–O bonds than any other $A$–O bond [40] as we will show below, making $BiPO_4$ more compressible than the rest of the studied monazite phosphates. The presence of lone pair on $Bi^{3+}$ may be a reason for this distinct behavior.

Calculations have let us determine the pressure dependence of the polyhedral volume and distortion for each compound. In the past, this information has allowed us to better understand the behavior of zircon-type phosphates under compression [14]. In figure 3, we compare the relative compression of the different polyhedra with that of the unit–cell volume. It can be observed that the $PO_4$ tetrahedron is highly incompressible in the four compounds. In contrast, the $AO_9$ polyhedron is much more

**Table 3.** Theoretical isothermal compressibility tensor coefficients, $\beta_{ij}$, and their eigenvalues, $\lambda_i$, and eigenvectors, $ev_i$, for several monazite-type phosphates at ambient pressure. The results were obtained using the finite Eulerian method.

| Compound | $LaPO_4$ | $CePO_4$ | $PrPO_4$ | $BiPO_4$ |
|---|---|---|---|---|
| $\beta_{11}$ ($10^{-3}$ GPa$^{-1}$) | 3.60 | 3.41 | 3.37 | 3.40 |
| $\beta_{22}$ ($10^{-3}$ GPa$^{-1}$) | 3.00 | 2.90 | 2.78 | 2.71 |
| $\beta_{33}$ ($10^{-3}$ GPa$^{-1}$) | 2.16 | 2.18 | 2.18 | 2.73 |
| $\beta_{13}$ ($10^{-3}$ GPa$^{-1}$) | $-1.30$ | $-1.22$ | $-0.91$ | $-1.10$ |
| $\lambda_1$ ($10^{-3}$ GPa$^{-1}$) | 4.37 | 4.16 | 3.86 | 4.21 |
| $ev_1$ ($\lambda_1$) | (0.861, 0, $-0.508$) | (0.851, 0, $-0.524$) | (0.879, 0, $-0.477$) | (0.803, 0, $-0.596$) |
| $\lambda_2$ ($10^{-3}$ GPa$^{-1}$) | 3.00 | 2.90 | 2.78 | 2.71 |
| $ev_2$ ($\lambda_2$) | (0, 1, 0) | (0, 1, 0) | (0, 1, 0) | (0, 1, 0) |
| $\lambda_3$ ($10^{-3}$ GPa$^{-1}$) | 1.39 | 1.43 | 1.69 | 1.92 |
| $ev_3$ ($\lambda_3$) | (0.508, 0, 0.861) | (0.524, 0, 0.851) | (0.477, 0, 0.879) | (0.596, 0, 0.803) |
| $\Psi$ (°)[a] | 120.5 | 121.6 | 118.5 | 126.6 |

[a] The major compression direction occurs in the (0 1 0) plane at the given angle $\Psi$ to the *c*-axis (from **c** to **a**).

compressible in all of them. In fact, the volume change of the $AO_9$ polyhedron is responsible for most of the volume decrease induced by pressure in the monazite-type oxides, as can be seen in figure 3. If the pressure dependence of the $PO_4$ volume is fitted with a third-order BM EOS, bulk moduli of 438(4), 436(4), 434(4), and 424(4) GPa are determined for $LaPO_4$, $CePO_4$, $PrPO_4$, and $BiPO_4$, respectively. These values are larger than the bulk modulus of many ultra-incompressible materials (e.g. $B_0 < 400$ GPa in cubic BN) [41, 42]. In contrast, the bulk moduli of the $AO_9$ polyhedra are 120(1), 122(1), 124(1), and 108(1) GPa for $LaO_9$, $CeO_9$, $PrO_9$, and $BiO_9$, respectively. These are similar to the bulk moduli of the corresponding oxides. Thus, in the studied compounds, $B_0$ can be properly described with the model proposed by Recio *et al* for oxides [43], in which the bulk compressibility is described in terms of the polyhedral compressibility. It is important to note here, that $BiO_9$ is the most compressible polyhedron among the four $AO_9$ polyhedra, tending to support the hypothesis that the Bi–O bonds make $BiPO_4$ to be the most compressible monazite-type phosphate.

The observed differential polyhedral compressibility provides also an explanation to the anisotropic compressibility of monazite-type oxides. The fact that $AO_9$ polyhedra are linked by stiff $PO_4$ tetrahedral units along the *c*-axis and *b*-axis, but interconnected directly along the *a*-axis (see figure 1), is what makes the *a*-axis to be more compressible than the other axes.

In order to analyze the influence of pressure on the shape of the polyhedra we calculated their polyhedral distortion using VESTA [44]. The results for the four compounds are shown in figure 4. It can be seen that $BiPO_4$ behaves differently than the other compounds. In $BiPO_4$, the distortion index of the $PO_4$ tetrahedron is reduced under pressure, unlike in the other three compounds; i.e. it becomes more regular. On the other hand, the distortion index of $BiO_9$ is permanently reduced by pressure decreasing from 0.054 at ambient pressure to 0.039 at 30 GPa. In contrast, the distortion index of the $AO_9$ polyhedron for $LaPO_4$, $CePO_4$, and $PrPO_4$ is first slightly reduced at low pressure and then considerably enhanced by compression, changing from approximately 0.030 at ambient pressure to a value close to 0.036 at 30 GPa and having a minimum distortion at a pressure close to 4 GPa (see figure 4).

### 4.2. Isothermal compressibility tensor

From the calculated pressure dependence of the unit-cell parameters of the four studied compounds, we determined the principal components of the isothermal compressibility tensor ($\beta_{ij}$) using the IRE (Institute of Radio Engineers) convention for the orthonormal basis of the tensor: $\mathbf{e}_3\|\mathbf{c}$, $\mathbf{e}_2\|\mathbf{b}*$, $\mathbf{e}_1\|\mathbf{e}_2 \times \mathbf{e}_3$. This is a second rank tensor that associates the state of strain of a crystal to the pressure applied to it. Analytical expressions have been developed to determine the coefficients ($\beta_{ij}$), eigenvalues ($\lambda_i$), and eigenvectors ($ev_i$) of the isothermal compressibility tensor for monoclinic crystals [45]. These expressions can be applied to monazite-type oxides. In our case, we used the Eulerian approximation [46] to calculate $\beta_{ij}$, $\lambda_i$, and $ev_i$ at ambient pressure, which are summarized in table 3, with the Win-Strain package [47]. We have found that the $\beta_{ij}$ coefficients follow a similar trend in $LaPO_4$, $CePO_4$, and $PrPO_4$, being $\beta_{11} > \beta_{22} > \beta_{33}$ in the three cases, while in $BiPO_4$ $\beta_{11} > \beta_{22} = \beta_{33}$ is obtained. The circumstance that $\beta_{11}$ is the largest coefficient follows from the large compressibility along the *a*-axis (see figure 2).

Taking into account the eigenvalues summarized in table 3, the values of the maximum, intermediate, and minimum compressibilities, for the four studied phosphates, can be determined. For instance, in $LaPO_4$ these values are $4.37 \times 10^{-3}$, $3.00 \times 10^{-3}$, and $1.39 \times 10^{-3}$ GPa$^{-1}$, respectively. A qualitatively similar picture has been obtained for the other three compounds. These results indicate that 50%, 49%, 46%, and 48% of the total compression of $LaPO_4$, $CePO_4$, $PrPO_4$, and $BiPO_4$, respectively, takes place along the direction of maximum compressibility.

On the other hand, from the eigenvector $ev_1$ (corresponding to the largest eigenvalue), the major compression direction can be determined. This direction is in the (0 1 0) plane for the four compounds, forming an angle $\Psi$ to the *c*-axis (from *c* to *a*); see table 3 for the values of $\Psi$. This direction is at 17°, 18, 15°, and 23° to the *a*-axis for $LaPO_4$, $CePO_4$, $PrPO_4$, and $BiPO_4$, respectively. The direction of intermediate compressibility (corresponding to $ev_2$) is along the *b*-axis in the four compounds, and the direction of minimum compressibility (corresponding to $ev_3$) is in the (0 1 0) plane at 90° to the
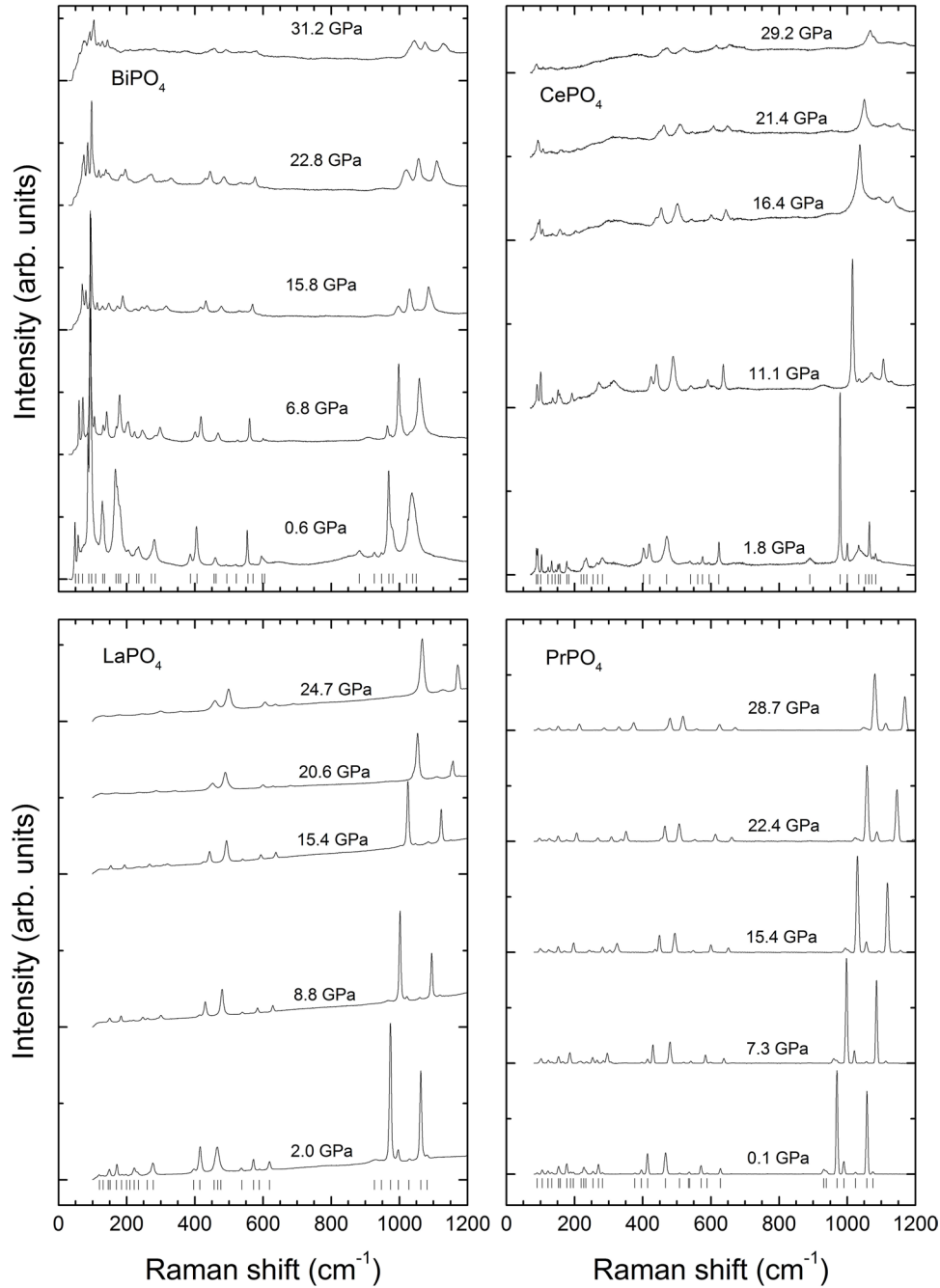
**Figure 5.** Selection of Raman spectra measured in the four phosphates at different pressures. The vertical ticks show the frequencies of the Raman modes identified at the lowest pressure.

direction of maximum compressibility. The results obtained for $BiPO_4$ agree well with those determined from powder XRD experiments [6]. Thus, the results reported here for the other three phosphates are the best estimations so far for the compressibility trends shown by monazite-type phosphates.

### 4.3. Raman-active vibrations

According to group theory analysis, the monazite structure has 72 vibrational modes at the zone center. Of them there are 36 optical Raman-active modes: $18A_g$ ($6T$, $3R$, $\nu_1$, $2\nu_2$, $3\nu_3$, $3\nu_4$) + $18B_g$ ($6T$, $3R$, $\nu_1$, $2\nu_2$, $3\nu_3$, $3\nu_4$); 33 optical IR-active modes: $17A_u$ ($5T$, $3R$, $\nu_1$, $2\nu_2$, $3\nu_3$, $3\nu_4$) + $16B_u$ ($4T$, $3R$, $\nu_1$,

$\nu_2$, $3\nu_3$, $3\nu_4$) and 3 acoustic modes: $1A_u$ ($T$) + $2B_u$ ($T$). These vibrational modes can be interpreted as 36 internal ($\nu_1$, $\nu_2$, $\nu_3$ and $\nu_4$) and 36 external (translational ($T$) and rotational ($R$)) modes of the $PO_4$ units of the monazite structure. In particular, the internal modes in monazite derive from the free $PO_4^{3-}$ molecule with $T_d$ symmetry: the symmetric stretching $A_1$ mode (aka $\nu_1$), the triply degenerated ($F_2$) asymmetric stretching (aka $\nu_3$), the doubly degenerated ($E$) bending mode (aka $\nu_2$) and the triply degenerated ($F_2$) bending mode (aka $\nu_4$), which are located at 938, 1017, 420 and 567 cm$^{-1}$, respectively [48]. It must be noted that in the monoclinic monazite structure, where the P atom occupies a $C_1$ symmetry, the degeneracies of the modes of the free $PO_4^{3-}$ molecule with $T_d$ symmetry are

**Table 4.** Experimental and calculated wave numbers ($\omega$) determined at ambient pressure for LaPO$_4$ including mode assignment. The linear (d$\omega$/d$P$) and quadratic (d$^2\omega$/d$P^2$) pressure coefficients are also reported as well as the experimental Grüneisen parameters ($\gamma$). The relative difference between measured and calculated frequencies ($R_\omega$) is given.

| Mode | Theory | | | | Experiment ($B_0 = 125$ GPa) | | | |
|---|---|---|---|---|---|---|---|---|
| | $\omega$ (cm$^{-1}$) | d$\omega$/d$P$ (cm$^{-1}$ Gpa$^{-1}$) | d$^2\omega$/d$P^2$ (cm$^{-1}$ GPa$^{-2}$) | $R_\omega$ | $\omega$ (cm$^{-1}$) | d$\omega$/d$P$ (cm$^{-1}$ GPa$^{-1}$) | d$^2\omega$/d$P^2$ (cm$^{-1}$ GPa$^{-2}$) | $\gamma$ |
| $B_g(T)$ | 86.3 | 0.23 | 0.01 | | | | | |
| $A_g(T)$ | 86.4 | 1.1 | −0.05 | | | | | |
| $A_g(T)$ | 98.3 | −0.2 | 0.02 | | | | | |
| $A_g(T)$ | 116.1 | −0.25 | 0.02 | 0.05 | 122 | 0.25 | 0.01 | 0.3 |
| $B_g(R)$ | 125.6 | 0.2 | 0.00 | 0.02 | 128 | 1.3 | 0.01 | 1.3 |
| $B_g(T)$ | 137.3 | 1.8 | −0.01 | | | | | |
| $A_g(R)$ | 143.3 | 0.5 | −0.01 | 0.00 | 143 | 1.6 | −0.01 | 1.4 |
| $A_g(R)$ | 146.3 | −0.3 | 0.02 | 0.04 | 152 | −0.8 | 0.05 | −0.7 |
| $B_g(T)$ | 163.8 | 1.3 | 0.01 | −0.04 | 158 | 3.5 | −0.01 | 2.8 |
| $B_g(R)$ | 175.5 | 3.6 | −0.02 | −0.03 | 170 | 3.8 | −0.03 | 2.8 |
| $A_g(T)$ | 182.5 | 3.8 | −0.06 | 0.00 | 183 | 3.6 | −0.08 | 2.5 |
| $B_g(T)$ | 208.8 | 3.8 | −0.03 | | | | | |
| $A_g(T)$ | 209.3 | 2.0 | 0.00 | 0.04 | 219 | 3.2 | 0.00 | 1.8 |
| $B_g(R)$ | 215.9 | 4.7 | −0.05 | 0.05 | 227 | 3.8 | 0.00 | 2.1 |
| $B_g(T)$ | 240.9 | 4.1 | −0.04 | −0.02 | 236 | 5.0 | −0.08 | 2.6 |
| $A_g(T)$ | 245.9 | 3.5 | −0.02 | 0.04 | 257 | 4.4 | −0.06 | 2.1 |
| $B_g(T)$ | 263.7 | 3.7 | −0.03 | 0.02 | 268 | 3.8 | −0.04 | 1.8 |
| $A_g(R)$ | 265.7 | 3.9 | −0.03 | 0.04 | 277 | 4.0 | −0.09 | 1.8 |
| $B_g(\nu_2)$ | 367.0 | 2.5 | −0.01 | 0.07 | 396 | 2.3 | −0.01 | 0.7 |
| $A_g(\nu_2)$ | 387.1 | 2.5 | −0.01 | 0.06 | 413 | 2.1 | 0.02 | 0.6 |
| $A_g(\nu_2)$ | 438.8 | 2.3 | −0.01 | 0.04 | 456 | 1.3 | −0.01 | 0.4 |
| $B_g(\nu_2)$ | 488.0 | 3.2 | −0.05 | −0.05 | 466 | 1.7 | 0.00 | 0.5 |
| $A_g(\nu_4)$ | 505.2 | 0.5 | 0.00 | −0.06 | 476 | 1.2 | −0.05 | 0.3 |
| $B_g(\nu_4)$ | 526.5 | 0.6 | 0.01 | 0.01 | 534 | 0.3 | 0.00 | 0.1 |
| $A_g(\nu_4)$ | 537.1 | 1.8 | −0.01 | | | | | |
| $B_g(\nu_4)$ | 555.6 | 1.8 | −0.01 | 0.03 | 570 | 1.6 | 0.00 | 0.4 |
| $A_g(\nu_4)$ | 585.5 | 1.3 | −0.01 | 0.00 | 588 | 2.2 | −0.01 | 0.5 |
| $B_g(\nu_4)$ | 587.0 | 1.4 | −0.01 | 0.05 | 619 | 1.0 | 0.00 | 0.2 |
| $B_g(\nu_1)$ | 923.4 | 3.9 | −0.03 | 0.00 | 923 | 3.3 | 0.02 | 0.4 |
| $A_g(\nu_1)$ | 929.6 | 4.0 | −0.03 | 0.01 | 940 | 2.8 | 0.03 | 0.4 |
| $A_g(\nu_3)$ | 958.6 | 3.7 | −0.01 | 0.01 | 968 | 4.2 | −0.03 | 0.5 |
| $A_g(\nu_3)$ | 984.3 | 4.0 | −0.03 | 0.00 | 987 | 4.2 | −0.03 | 0.5 |
| $B_g(\nu_3)$ | 989.4 | 4.5 | −0.03 | | | | | |
| $A_g(\nu_3)$ | 1020.5 | 4.7 | −0.05 | 0.00 | 1021 | 3.8 | 0.02 | 0.5 |
| $B_g(\nu_3)$ | 1028.2 | 3.6 | −0.01 | 0.02 | 1054 | 4.0 | 0.03 | 0.5 |
| $B_g(\nu_3)$ | 1036.5 | 5.2 | −0.03 | 0.03 | 1070 | 4.4 | 0.013 | 0.5 |

completely broken leading to nine internal modes. Besides, the number of vibrational modes in the monazite structure is twice that in the zircon structure—there are double number of formula units in the primitive unit cell of the monazite structure than in the zircon structure [49]—thus resulting in eighteen internal modes in the monazite structure.

The Raman spectra of many monazite-type phosphates at ambient conditions have been previously studied [27, 50, 51]. Thirty-three modes have been measured and assigned for BiPO$_4$ [27], while twenty-two or twenty-three modes have been measured at ambient pressure and assigned in LaPO$_4$, CePO$_4$, and PrPO$_4$ by different authors [50, 51]. As regards HP studies, around fourteen and sixteen Raman modes were studied in CePO$_4$ and LaPO$_4$, respectively, under compression

[11–13]. It must be stressed that a detailed assignment and discussion of the symmetry of the different vibrational modes of monazite-type oxides was not done in previous works.

A selection of Raman spectra measured under compression in different compounds can be seen in figure 5. At the bottom of each panel of the figure, vertical ticks mark the experimental phonon frequencies identified at the lowest pressure shown. Determined Raman frequencies at ambient pressure agree well with those previously reported [11–13, 27, 50, 51]. In the present Raman experiments, we have detected thirty-two modes for CePO$_4$, twenty-nine for LaPO$_4$, thirty-two for PrPO$_4$, and thirty-four for BiPO$_4$. It can be observed that the Raman spectrum of orthophosphate monazites can be divided into three regions: (i) the low-frequency region up to

**Table 5.** Experimental and calculated wave numbers ($\omega$) determined at ambient pressure for CePO$_4$ including mode assignment. The linear ($d\omega/dP$) and quadratic ($d^2\omega/dP^2$) pressure coefficients are also reported as well as the experimental Grüneisen parameters ($\gamma$). The relative difference between measured and calculated frequencies ($R_\omega$) is given.

| | Theory | | | | Experiment ($B_0 = 109$ GPa) | | | |
|---|---|---|---|---|---|---|---|---|
| Mode | $\omega$ (cm$^{-1}$) | $d\omega/dP$ (cm$^{-1}$ GPa$^{-1}$) | $d^2\omega/dP^2$ (cm$^{-1}$ GPa$^{-2}$) | $R_\omega$ | $\omega$ (cm$^{-1}$) | $d\omega/dP$ (cm$^{-1}$ GPa$^{-1}$) | $d^2\omega/dP^2$ (cm$^{-1}$ GPa$^{-2}$) | $\gamma$ |
| $B_g(T)$ | 85.8 | 0.2 | 0.01 | 0.02 | 88 | 0.1 | 0.01 | 0.1 |
| $A_g(T)$ | 88.7 | 1.1 | −0.05 | 0.04 | 92 | 1.2 | −0.04 | 1.4 |
| $A_g(T)$ | 100.8 | −0.1 | 0.01 | 0.01 | 102 | −0.1 | 0.01 | −0.1 |
| $A_g(T)$ | 123.3 | −0.2 | 0.01 | −0.02 | 121 | 1.0 | −0.03 | 0.9 |
| $B_g(R)$ | 128.8 | 0.1 | 0.00 | 0.02 | 131 | 0.6 | −0.02 | 0.5 |
| $B_g(T)$ | 143.1 | 0.1 | 0.02 | 0.00 | 143 | 0.9 | −0.02 | 0.7 |
| $A_g(R)$ | 145.8 | 1.5 | 0.00 | 0.03 | 151 | 0.9 | 0.02 | 0.6 |
| $B_g(T)$ | 149.8 | −0.3 | 0.03 | 0.05 | 158 | −0.2 | 0.02 | −0.1 |
| $B_g(R)$ | 169.1 | 1.3 | 0.01 | 0.03 | 175 | 1.3 | 0.00 | 0.8 |
| $A_g(R)$ | 183.3 | 3.7 | −0.03 | 0.00 | 183 | 2.5 | −0.01 | 1.5 |
| $A_g(T)$ | 193.9 | 3.7 | −0.06 | | | | | |
| $B_g(T)$ | 219.0 | 2.2 | −0.01 | 0.00 | 219 | 3.8 | −0.04 | 1.8 |
| $A_g(T)$ | 221.4 | 3.9 | −0.03 | 0.02 | 227 | 3.8 | −0.01 | 1.8 |
| $B_g(R)$ | 228.4 | 4.8 | −0.04 | 0.03 | 236 | 3.0 | −0.02 | 1.4 |
| $A_g(T)$ | 255.2 | 4.2 | −0.03 | 0.00 | 254 | 4.8 | 0.00 | 2.1 |
| $B_g(T)$ | 261.5 | 3.7 | −0.03 | | | | | |
| $A_g(R)$ | 277.4 | 3.5 | −0.03 | −0.02 | 268 | 2.9 | 0.01 | 1.2 |
| $B_g(T)$ | 278.4 | 3.9 | −0.04 | −0.02 | 282 | 2.5 | 0.00 | 1.0 |
| $B_g(\nu_2)$ | 374.8 | 2.8 | −0.01 | 0.07 | 402 | 2.7 | −0.02 | 0.7 |
| $A_g(\nu_2)$ | 392.1 | 2.7 | −0.02 | 0.05 | 414 | 2.7 | −0.02 | 0.7 |
| $A_g(\nu_2)$ | 451.7 | 2.6 | −0.02 | 0.03 | 467 | 2.2 | 0.01 | 0.5 |
| $B_g(\nu_2)$ | 493.6 | 3.2 | −0.05 | | | | | |
| $A_g(\nu_4)$ | 508.7 | 0.7 | −0.01 | | | | | |
| $B_g(\nu_4)$ | 530.4 | 0.8 | 0.01 | 0.01 | 536 | 0.6 | −0.01 | 0.1 |
| $A_g(\nu_4)$ | 540.9 | 2.0 | −0.01 | 0.04 | 561 | 1.0 | 0.02 | 0.2 |
| $B_g(\nu_4)$ | 558.2 | 1.9 | −0.01 | 0.02 | 572 | 1.9 | −0.01 | 0.4 |
| $A_g(\nu_4)$ | 592.5 | 1.5 | −0.01 | −0.00 | 590 | 1.2 | 0.00 | 0.2 |
| $B_g(\nu_4)$ | 594.4 | 1.6 | −0.01 | 0.04 | 620 | 1.6 | −0.01 | 0.3 |
| $B_g(\nu_1)$ | 926.1 | 4.1 | −0.03 | −0.04 | 890 | 2.9 | −0.01 | 0.4 |
| $A(\nu_1)$ | 933.03 | 4.1 | −0.03 | 0.04 | 972 | 4.5 | −0.04 | 0.5 |
| $A_g(\nu_3)$ | 963.7 | 3.8 | −0.01 | 0.03 | 994 | 4.3 | −0.04 | 0.5 |
| $A_g(\nu_3)$ | 992.0 | 4.7 | −0.03 | 0.04 | 1034 | 3.9 | −0.02 | 0.4 |
| $B_g(\nu_3)$ | 995.94 | 3.8 | −0.02 | 0.05 | 1046 | 5.6 | −0.05 | 0.6 |
| $A_g(\nu_3)$ | 1029.3 | 4.8 | −0.02 | 0.03 | 1064 | 4.2 | −0.01 | 0.4 |
| $B_g(\nu_3)$ | 1035.9 | 3.6 | −0.02 | 0.04 | 1075 | 3.8 | −0.00 | 0.4 |
| $B_g(\nu_3)$ | 1044.1 | 5.5 | −0.03 | 0.04 | 1084 | 3.8 | −0.00 | 0.4 |

300 cm$^{-1}$, corresponding to the eighteen external or lattice $T$ and $R$ modes: $9A_g$ ($6T,3R$) + $9B_g$ ($6T,3R$); (ii) the medium-frequency region between 400 and 650 cm$^{-1}$, corresponding to the ten internal bending modes deriving from $\nu_2$ and $\nu_4$ modes: $5A_g$ ($2\nu_2$, $3\nu_4$) + $5B_g$ ($2\nu_2$, $3\nu_4$); and (iii) the high-frequency region above 900 cm$^{-1}$ corresponding to the eight internal stretching modes deriving from $\nu_1$ and $\nu_3$ modes: $4A_g$ ($\nu_1$, $3\nu_3$) + $4B_g$ ($\nu_1$, $3\nu_3$). This assignment is consistent with the observation that the frequencies at ambient pressure in the high-frequency region are not very sensitive to a change in the trivalent cation. Curiously, a phonon gap is observed between all these regions in phosphates, which is also observed in the monazite structure of chromates and selenates [38]; however, a mixing of lattice and $\nu_2$ bending modes in the monazite

structure of vanadates is observed [52, 53]. This feature is also observed in many $ABO_4$ compounds with zircon structure [49].

The symmetry assignment of the experimental Raman modes (see tables 4–7) has been made through the comparison of experimental and theoretical frequencies and pressure coefficients and through visualization of atomic vibrations with the program J-ICE using the OUTCAR file of VASP [54]. Our symmetry assignment has partial agreement with the one made from polarized Raman measurements at ambient pressure [50, 51]. It can be stressed that the two internal stretching modes with lowest frequency (below 950 cm$^{-1}$ in the three compounds) correspond to the $A_g$ ($\nu_1$) + $B_g$ ($\nu_1$) modes, where oxygen atoms vibrate symmetrically around P atoms. On the

**Table 6.** Experimental and calculated wave numbers ($\omega$) determined at ambient pressure for PrPO$_4$ including mode assignment. The linear (d$\omega$/d$P$) and quadratic (d$^2\omega$/d$P^2$) pressure coefficients are also reported as well as the experimental Grüneisen parameters ($\gamma$). The relative difference between measured and calculated frequencies ($R_\omega$) is given.

| | Theory | | | | Experiment ($B_0 = 120$ GPa) | | | |
|---|---|---|---|---|---|---|---|---|
| Mode | $\omega$ (cm$^{-1}$) | d$\omega$/d$P$ (cm$^{-1}$ GPa$^{-1}$) | d$^2\omega$/d$P^2$ (cm$^{-1}$ GPa$^{-2}$) | $R_\omega$ | $\omega$ (cm$^{-1}$) | d$\omega$/d$P$ (cm$^{-1}$ GPa$^{-1}$) | d$^2\omega$/d$P^2$ (cm$^{-1}$ GPa$^{-2}$) | $\gamma$ |
| $B_g(T)$ | 87.3 | 0.2 | 0.01 | | | | | |
| $A_g(T)$ | 89.8 | 1.1 | $-0.05$ | 0.00 | 90 | 1.1 | $-0.04$ | 1.5 |
| $A_g(T)$ | 103.8 | $-0.2$ | 0.02 | 0.01 | 105 | $-0.4$ | 0.02 | $-0.5$ |
| $A_g(T)$ | 124.9 | $-0.3$ | 0.02 | $-0.02$ | 122 | 0.1 | 0.00 | 0.1 |
| $B_g(R)$ | 131.5 | 0.2 | 0.00 | 0.01 | 133 | 0.1 | 0.00 | 0.1 |
| $B_g(T)$ | 143.2 | 1.8 | $-0.01$ | | | | | |
| $A_g(R)$ | 149.1 | 0.5 | $-0.01$ | 0.03 | 153 | 1.5 | $-0.02$ | 1.2 |
| $B_g(T)$ | 155.2 | $-0.3$ | 0.02 | 0.02 | 158 | $-0.7$ | 0.03 | $-0.5$ |
| $B_g(R)$ | 173.6 | 1.3 | 0.01 | $-0.00$ | 173 | 1.4 | 0.00 | 1.0 |
| $A_g(R)$ | 183.2 | 3.6 | $-0.02$ | $-0.01$ | 182 | 3.2 | 0.01 | 2.1 |
| $A_g(T)$ | 193.7 | 3.8 | $-0.06$ | 0.01 | 196 | 2.8 | 0.02 | 1.7 |
| $B_g(T)$ | 223.8 | 3.8 | $-0.03$ | $-0.02$ | 219 | 2.2 | 0.02 | 1.2 |
| $A_g(T)$ | 224.9 | 2.0 | 0.00 | 0.01 | 227 | 3.8 | $-0.02$ | 2.0 |
| $B_g(R)$ | 232.5 | 4.7 | $-0.05$ | 0.00 | 233 | 5.1 | $-0.06$ | 2.6 |
| $A_g(T)$ | 259.5 | 4.1 | $-0.04$ | $-0.01$ | 258 | 4.0 | $-0.02$ | 1.9 |
| $B_g(T)$ | 264.8 | 3.5 | $-0.02$ | 0.02 | 270 | 5.1 | $-0.09$ | 2.3 |
| $B_g(T)$ | 281.8 | 3.7 | $-0.03$ | | | | | |
| $A_g(R)$ | 284.4 | 3.9 | $-0.03$ | $-0.01$ | 282 | 3.0 | $-0.01$ | 1.3 |
| $B_g(\nu_2)$ | 376.9 | 2.5 | $-0.01$ | 0.00 | 377 | 2.8 | 0.00 | 0.9 |
| $A_g(\nu_2)$ | 395.4 | 2.5 | $-0.01$ | 0.00 | 396 | 2.5 | 0.00 | 0.8 |
| $A_g(\nu_2)$ | 454.6 | 2.3 | $-0.01$ | $-0.10$ | 414 | 2.4 | $-0.01$ | 0.7 |
| $B_g(\nu_2)$ | 497.0 | 3.2 | $-0.05$ | $-0.06$ | 467 | 1.8 | 0.00 | 0.5 |
| $A_g(\nu_4)$ | 510.0 | 0.5 | 0.00 | 0.00 | 508 | 1.8 | $-0.02$ | 0.4 |
| $B_g(\nu_4)$ | 532.7 | 0.6 | 0.01 | 0.00 | 534 | 0.9 | 0.00 | 0.2 |
| $A_g(\nu_4)$ | 542.7 | 1.8 | $-0.01$ | $-0.01$ | 538 | 1.8 | 0.00 | 0.4 |
| $B_g(\nu_4)$ | 560.9 | 1.8 | $-0.01$ | 0.02 | 571 | 1.8 | 0.00 | 0.4 |
| $A_g(\nu_4)$ | 595.8 | 1.3 | $-0.01$ | $-0.01$ | 591 | 1.7 | $-0.04$ | 0.3 |
| $B_g(\nu_4)$ | 598.1 | 1.4 | $-0.01$ | 0.05 | 628 | 1.5 | 0.00 | 0.3 |
| $B_g(\nu_1)$ | 930.4 | 3.9 | $-0.03$ | 0.00 | 931 | 4.0 | 0.00 | 0.5 |
| $A_g(\nu_1)$ | 938.3 | 4.0 | $-0.03$ | 0.00 | 939 | 4.1 | 0.00 | 0.5 |
| $A_g(\nu_3)$ | 967.6 | 3.7 | $-0.01$ | 0.00 | 970 | 3.8 | 0.00 | 0.5 |
| $A_g(\nu_3)$ | 995.3 | 4.0 | $-0.03$ | $-0.01$ | 990 | 4.3 | 0.00 | 0.5 |
| $B_g(\nu_3)$ | 1000.7 | 4.5 | $-0.03$ | | | | | |
| $A_g(\nu_3)$ | 1033.4 | 4.7 | $-0.05$ | $-0.01$ | 1024 | 4.5 | 0.00 | 0.5 |
| $B_g(\nu_3)$ | 1040.2 | 3.6 | $-0.01$ | 0.02 | 1058 | 3.9 | 0.00 | 0.4 |
| $B_g(\nu_3)$ | 1049.2 | 5.2 | $-0.03$ | 0.02 | 1075 | 5.3 | 0.00 | 0.6 |

other hand, the six internal stretching modes with highest frequency (above 950 cm$^{-1}$ in the three compounds) correspond to the $3A_g$ ($\nu_3$) + $3B_g$ ($\nu_3$) modes, where oxygen atoms vibrate asymmetrically around P atoms. This assignment is also valid for IR-active stretching modes. Support for this assignment comes from the frequencies of the symmetric $\nu_1$ and the asymmetric $\nu_3$ modes in the free PO$_4^{3-}$ molecule previously commented. In particular, the most intense mode in the high-frequency region correspond to a symmetric stretching $A_g(\nu_1)$ mode and the second most intense mode is an antisymmetric stretching $B_g(\nu_3)$ mode. The same reasoning used above for the high-frequency region allows us to assign the O-P-O bending modes in the medium-frequency region. Namely, the

6 internal modes with highest frequency correspond to the $3A_g$ ($\nu_4$) + $3B_g$ ($\nu_4$) modes, where P atoms move, and the 4 internal bending modes with lowest frequency correspond to the $2A_g$ ($\nu_2$) + $2B_g$ ($\nu_2$) modes, where P atoms are almost static.

On the above reasoning, we can establish a comparison with previous works. Tables 4–7 show that all modes above 350 cm$^{-1}$ are internal ones, unlike in previous works, where two modes around 396 and 414 cm$^{-1}$ in CePO$_4$ (at similar frequencies in other phosphates) were considered lattice or external modes [11, 51]. Similarly, modes at 968 and 987 cm$^{-1}$ in LaPO$_4$ (at similar frequencies in other phosphates) correspond to asymmetric stretching modes that were previously assigned to symmetric stretching modes [12] or

**Table 7.** Experimental and calculated wave numbers ($\omega$) determined at ambient pressure for $BiPO_4$ including mode assignment. The linear ($d\omega/dP$) and quadratic ($d^2\omega/dP^2$) pressure coefficients are also reported as well as the experimental Grüneisen parameters ($\gamma$). The relative difference between measured and calculated frequencies ($R_\omega$) is given.

| | Theory | | | | Experiment ($B_0 = 117\,GPa$) | | | |
|---|---|---|---|---|---|---|---|---|
| Mode | $\omega$ (cm$^{-1}$) | $d\omega/dP$ (cm$^{-1}$ GPa$^{-1}$) | $d^2\omega/dP^2$ (cm$^{-1}$ GPa$^{-2}$) | $R_\omega$ | $\omega$ (cm$^{-1}$) | $d\omega/dP$ (cm$^{-1}$ GPa$^{-1}$) | $d^2\omega/dP^2$ (cm$^{-1}$ GPa$^{-2}$) | $\gamma$ |
| $B_g(T)$ | 58.2 | 1.9 | −0.02 | −0.12 | 51 | 1.9 | −0.02 | 4.4 |
| $A_g(T)$ | 68.4 | 1.5 | −0.05 | −0.12 | 60 | 1.8 | −0.02 | 3.5 |
| $A_g(T)$ | 73.3 | −0.1 | 0.02 | −0.04 | 70 | −0.1 | 0.01 | −0.2 |
| $B_g(R)$ | 89.3 | 1.1 | −0.02 | 0.01 | 90 | 1.0 | 0.00 | 1.3 |
| $A_g(T)$ | 95.3 | 0.8 | −0.01 | 0.02 | 97 | −0.1 | 0.01 | −0.1 |
| $B_g(T)$ | 102.6 | 1.2 | −0.01 | 0.06 | 108 | 0.9 | 0.00 | 1.0 |
| $A_g(R)$ | 132.7 | 1.4 | −0.06 | −0.01 | 131 | 2.2 | −0.08 | 2.0 |
| $B_g(T)$ | 134.7 | −1.1 | 0.05 | 0.01 | 135 | −0.5 | 0.02 | −0.4 |
| $A_g(R)$ | 165.7 | −0.3 | 0.03 | 0.03 | 170 | −0.1 | 0.02 | −0.1 |
| $B_g(R)$ | 167.8 | 1.3 | 0.00 | 0.05 | 177 | 1.2 | −0.01 | 0.8 |
| $A_g(T)$ | 168.4 | 1.6 | 0.01 | | | | | |
| $A_g(T)$ | 184.0 | 3.9 | −0.04 | −0.01 | 183 | 3.8 | −0.04 | 2.4 |
| $B_g(R)$ | 185.2 | 4.1 | −0.03 | | | | | |
| $B_g(T)$ | 203.9 | 3.5 | −0.02 | 0.02 | 207 | 2.9 | −0.02 | 1.6 |
| $B_g(T)$ | 226.2 | 4.1 | −0.03 | 0.02 | 230 | 4.2 | 0.00 | 2.1 |
| $A_g(T)$ | 231.9 | 2.3 | −0.01 | 0.02 | 237 | 1.8 | −0.01 | 0.9 |
| $B_g(T)$ | 271.3 | 2.2 | −0.01 | 0.01 | 272 | 3.2 | 0.00 | 1.4 |
| $A_g(R)$ | 278.7 | 2.6 | −0.02 | 0.01 | 283 | 2.9 | −0.03 | 1.2 |
| $B_g(\nu_2)$ | 368.3 | 2.6 | −0.01 | 0.05 | 388 | 2.3 | −0.02 | 0.7 |
| $A_g(\nu_2)$ | 384.5 | 2.5 | −0.01 | 0.06 | 407 | 2.0 | −0.01 | 0.6 |
| $A_g(\nu_2)$ | 438.7 | 1.7 | −0.01 | 0.04 | 457 | 1.7 | 0.00 | 0.4 |
| $B_g(\nu_2)$ | 469.9 | 2.7 | −0.03 | −0.01 | 464 | 1.7 | −0.01 | 0.4 |
| $A_g(\nu_4)$ | 499.0 | 0.9 | −0.01 | −0.01 | 496 | 1.5 | 0.00 | 0.4 |
| $A_g(\nu_4)$ | 527.2 | 0.6 | 0.00 | −0.01 | 523 | 1.2 | −0.03 | 0.3 |
| $B_g(\nu_4)$ | 527.3 | 1.3 | 0.00 | 0.06 | 557 | 1.3 | −0.01 | 0.3 |
| $B_g(\nu_4)$ | 540.9 | 1.6 | 0.00 | 0.06 | 572 | 1.6 | 0.00 | 0.3 |
| $A_g(\nu_4)$ | 568.1 | 1.1 | −0.01 | 0.05 | 598 | 1.0 | −0.01 | 0.2 |
| $B_g(\nu_4)$ | 573.9 | 1.4 | −0.01 | 0.05 | 604 | 1.1 | −0.02 | 0.2 |
| $A_g(\nu_1)$ | 911.9 | 4.4 | −0.04 | −0.03 | 883 | 4.1 | −0.01 | 0.5 |
| $B_g(\nu_1)$ | 915.8 | 4.6 | −0.05 | 0.01 | 926 | 5.3 | −0.05 | 0.7 |
| $A_g(\nu_3)$ | 935.3 | 5.5 | −0.04 | 0.01 | 948 | 5.8 | −0.11 | 0.7 |
| $A_g(\nu_3)$ | 956.5 | 4.2 | −0.01 | 0.01 | 970 | 4.8 | −0.04 | 0.6 |
| $B_g(\nu_3)$ | 962.3 | 5.3 | −0.05 | 0.02 | 981 | 4.4 | −0.03 | 0.5 |
| $B_g(\nu_3)$ | 985.3 | 4.0 | −0.01 | 0.04 | 1021 | 4.7 | −0.07 | 0.5 |
| $A_g(\nu_3)$ | 1010.1 | 4.1 | −0.01 | 0.03 | 1039 | 3.8 | −0.03 | 0.4 |
| $B_g(\nu_3)$ | 1016.6 | 4.5 | −0.02 | 0.03 | 1050 | 3.8 | −0.03 | 0.4 |

not previously defined [11, 50, 51]. In tables 4–7, we have also included mode Grüneisen parameters [55], which were calculated using the bulk moduli given in table 2, and the parameter $R_\omega$, which is the relative difference between measured and calculated frequencies [56]. For $LaPO_4$ the difference between experimental and theoretical frequencies at ambient pressure is smaller than 7%, in $CePO_4$ smaller than 7%, in $PrPO_4$ smaller than 10%, and in $BiPO_4$ smaller than 12%, respectively. There is a tendency for a small underestimation of the calculated frequencies and in all the compounds the agreement is slightly better for the high-frequency modes than for the low-frequency modes.

It can be observed in figure 5 that the whole Raman spectrum of the four compounds at all pressures can be assigned to the monazite structure with no evidence of phase transitions or chemical decomposition. Only a shift of the Raman modes, a gradual decrease of the Raman signal intensity, and a gradual broadening of the peaks, likely due to the loss of hydrostaticity beyond 10 GPa, were observed in monazite under compression in the pressure range studied. In this context and with the overlapping of several Raman modes induced by pressure, fewer Raman modes were observed at the highest pressure in each compound: only eleven modes in $LaPO_4$, fourteen in $CePO_4$, eighteen in $PrPO_4$, and fifteen in $BiPO_4$.
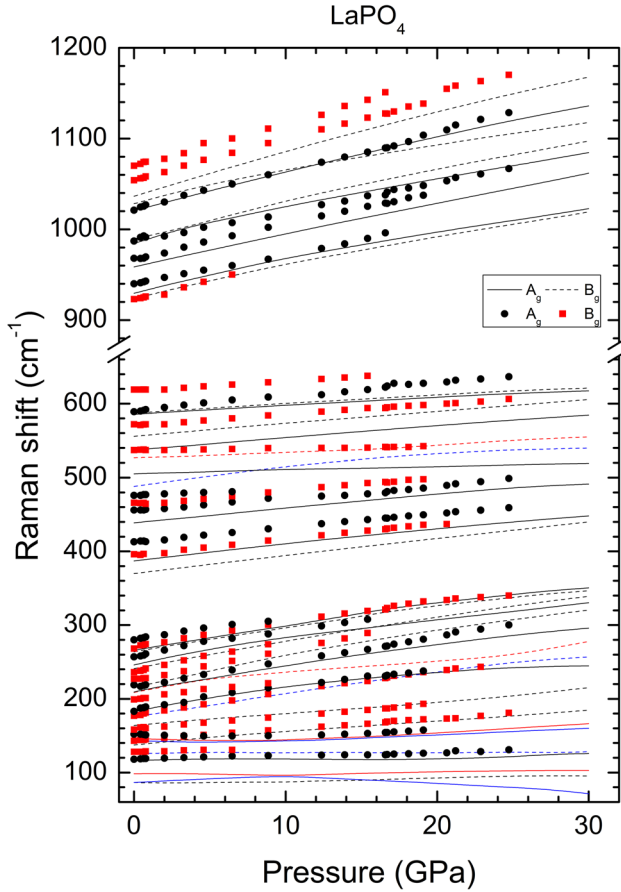
**Figure 6.** Pressure dependence of the Raman modes of LaPO$_4$. Different color and symbols (experiments) and type of lines (calculations) have been used for $A_g$ and $B_g$ modes. Blue and red have been used to identify anti-crossing modes.
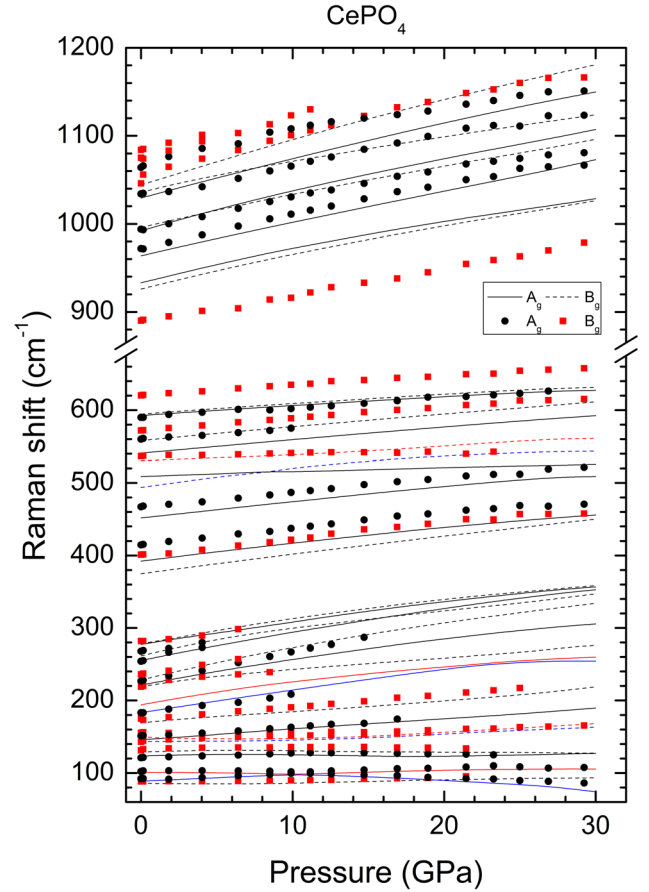
**Figure 7.** Pressure dependence of the Raman modes of CePO$_4$. Different color and symbols (experiments) and type of lines (calculations) have been used for $A_g$ and $B_g$ modes. Blue and red have been used to identify anti-crossing modes.

As can been seen in figures 6–9, which show the experimental and theoretical pressure dependence of the Raman-active mode frequencies, most modes harden under compression. However, there are a few lattice modes around 100 and 150 cm$^{-1}$ whose frequencies decrease under compression (aka soft modes). There are also modes of the same symmetry that show an anti-crossing behavior. The pressure dependence of the modes can be described either by a linear or by a quadratic function (depending on the mode). Consequently, we have summarized the Raman mode frequencies and their pressure coefficients at ambient pressure in tables 4–7. A rather good agreement is found between the experimental and theoretical frequencies and pressure coefficients despite the overall underestimation of vibrational frequencies in the calculations.

As regards the internal stretching modes of the PO$_4$ tetrahedron, they have similar pressure coefficients being among the modes whose frequency increases faster under compression. In contrast, bending motions of the PO$_4$ tetrahedron have smaller, and not so similar, pressure coefficients. In particular, the two modes with frequencies between 500 and 530 cm$^{-1}$ at ambient pressure in all the compounds are the less affected by pressure. On the other hand, the mode most sensitive to pressure in this region is a B$_g$ mode with a frequency smaller than 500 cm$^{-1}$ at ambient pressure. Due to the different pressure

dependence, the crossover of $A_g$ and $B_g$ modes is observed in figures 6–9. Interestingly, there is also an anti-crossing of two $B_g$ modes (identified in red and blue in the figures) in the three lanthanide phosphates; i.e. the consequent convergence and divergence of their frequencies, with a change in their pressure dependences at similar pressures. This behavior might be related to the non-isotropic compression of monazite, which could make the lower-frequency $B_g$ mode to move faster towards high frequency than the higher frequency mode. An extrapolation of the low-pressure behavior of both modes will make their frequencies to match at the critical pressure. However, since these two vibrations share the same irreducible representation, they cannot be degenerate and consequently the anti-crossing phenomenon exist [57].

Finally, external or lattice modes involve movements of the trivalent cation and their frequencies severely depend upon the mass of the *A* atom. In particular, the lowest frequency modes among the four compounds are in BiPO$_4$. This is because this compound has the heavy Bi atoms. This behavior is analogous to that previously observed in related oxides [58]. These external modes of the monazite structure show quite different pressure coefficients since they involve different *A*–O bonds, some of them very compressible while others not [4]. In the low-frequency region, the differences among the pressure dependence of different modes are also
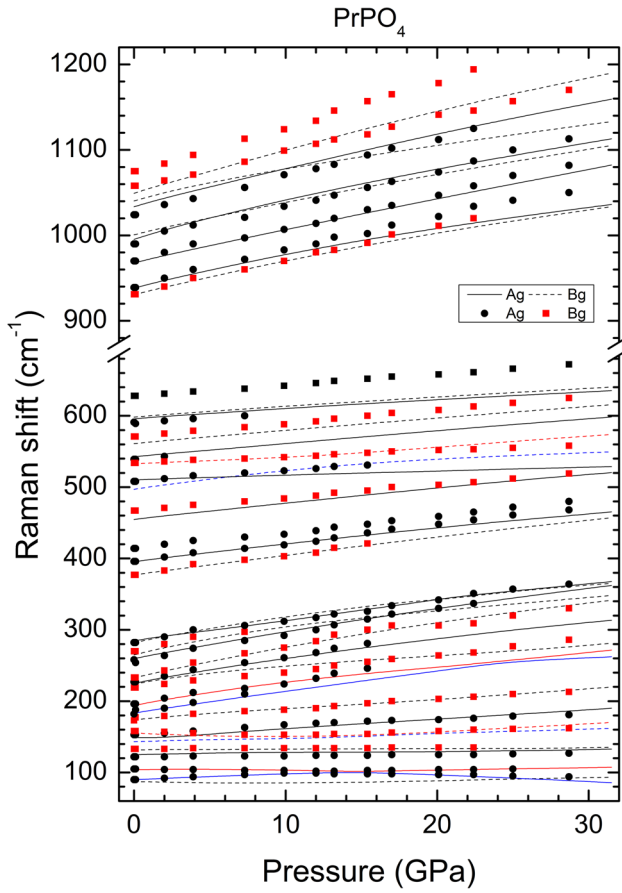
**Figure 8.** Pressure dependence of the Raman modes of PrPO$_4$. Different color and symbols (experiments) and type of lines (calculations) have been used for $A_g$ and $B_g$ modes. Blue and red have been used to identify anti-crossing modes.

**Figure 9.** Pressure dependence of the Raman modes of BiPO$_4$. Different color and symbols (experiments) and type of lines (calculations) have been used for $A_g$ and $B_g$ modes. Blue and red have been used to identify anti-crossing modes.

quite notable. Consequently, more crossing and anti-crossing phenomena are observed in this region. In particular, it is interesting the behavior of the two lowest frequency $A_g$ modes in the four compounds (for instance the modes with wavenumber 86.4 and 98.3 cm$^{-1}$ in LaPO$_4$). In all of them, a phonon anti-crossing is observed. As a consequence, after a critical pressure, the lowest-frequency $A_g$ mode becomes gradually softer under compression, becoming its frequency even smaller than the lowest-frequency mode at ambient pressure (a $B_g$ mode) as shown in tables 4 to 7. We believe the gradual softening of this mode could be related to a pressure-driven instability of the monazite structure, which occurs after this phenomenon is triggered in the four compounds. The two low-frequency $A_g$ vibrations correspond to atomic movements in which two trivalent atoms linked to corners of the PO$_4$ tetrahedron make twisting or waging movements. The twisting movement is associated to the mode that gradually softens after the critical pressure. The presence of such modes has been proposed to be related with pressure-driven instabilities of monazite chromates [59] and related compounds [60–62]. The possible relation of these soft modes with the phase transition that occurs near 30 GPa in monazite phosphates deserves to be studied in the future.
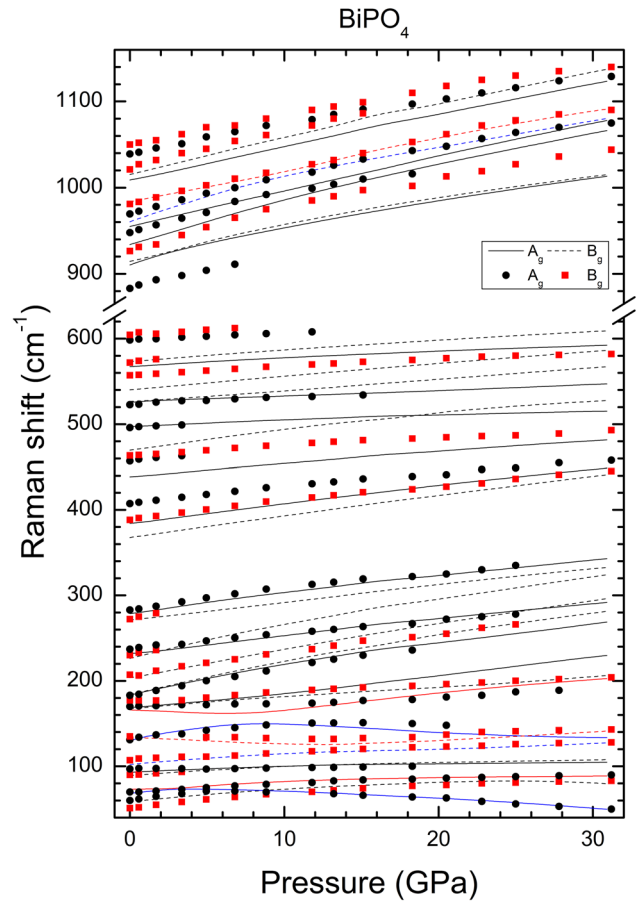
## 5. Concluding remarks

We have theoretically studied the pressure effects on the crystal structure of monazite-type LaPO$_4$, CePO$_4$, PrPO$_4$, and BiPO$_4$. In particular, this is the first time that high pressure studies are carried out in PrPO$_4$. We have determined the equations of state as well as polyhedral compressibilities of the four monazites and reported how their polyhedral units are distorted under compression. In addition, we have calculated the isothermal compressibility tensor in these monazites and determined the direction of maximum compression. We have also theoretically and experimentally studied the Raman-active modes of the four monazites under compression and provided an accurate assignment of their Raman-active mode symmetries. The behavior of the different Raman-active modes as a function of pressure has been analyzed. In this way, we have identified several modes that gradually soften with pressure in the four phosphates and several couples of anti-crossing modes. As expected, Raman scattering measurements confirm that there is no phase transition up to the highest pressure covered by the studies; a result that is in good agreement with previous x-ray diffraction measurements.

## Acknowledgments

## ORCID iDs

D Errandonea  https://orcid.org/0000-0003-0189-4221
O Gomis  https://orcid.org/0000-0001-6763-0638
S N Achary  https://orcid.org/0000-0002-2103-1063

## References

[1] Ni Y, Hughes J M and Mariano A N 1995 *Am. Mineral.* **80** 21–6
[2] Clavier N, Podor R and Dacheux N 2011 *J. Eur. Ceram. Soc.* **31** 941–76
[3] Errandonea D 2017 *Phys. Status Solidi* b **254** 1700016
[4] Lacomba-Perales R, Errandonea D, Meng Y and Bettinelli M 2010 *Phys. Rev.* B **81** 064113
[5] Ruiz-Fuertes J, Hirsch A, Friedrich A, Winkler B, Bayarjargal L, Morgenroth W, Peters L, Roth G and Milman V 2016 *Phys. Rev.* B **94** 134109
[6] Errandonea D, Gomis O, Santamaría-Perez D, García-Domene B, Muñoz A, Rodríguez-Hernández P, Achary S N, Tyagi A K and Popescu C 2015 *J. Appl. Phys.* **117** 105902
[7] Achary S N, Bevara S and Tyagi A K 2017 *Coord. Chem. Rev.* **340** 266–97
[8] Wilkinson T M, Wu D, Musselman M A, Li N, Mara N and Packard C E 2017 *Mater. Sci. Eng.* A **691** 203–10
[9] Heffernan K M, Ross N L, Spencer E C and Boatner L 2016 *J. Solid Stat. Chem.* **241** 180–6
[10] Feng J, Xiao B, Zhou R and Pan W 2013 *Acta Mater.* **61** 7364–83
[11] Huang T, Lee J S, Kung J and Lin C M 2010 *Sol. State Commun.* **150** 1845–50
[12] Zhao Z, Zhang X, Zuo J and Ding Z 2010 *J. Nanosci. Nanotechnol.* **10** 7791–4
[13] Zhao Z, Zuo J and Ding Z 2010 *J. Rare Earths* **28** 254–7
[14] Gomis O, Lavina B, Rodriguez-Hernandez P, Muñoz A, Errandonea R, Errandonea D and Bettinelli M 2017 *J. Phys.: Condens. Matter* **29** 095401
[15] Errandonea D *et al* 2016 *J. Phys. Chem.* C **120** 13749–62
[16] Errandonea D, Muñoz A, Rodriguez-Hernandez P, Gomis O, Achary S N, Popescu C, Patwe S J and Tyagi A K 2016 *Inorg. Chem.* **55** 4958–69
[17] Hohenberg P and Kohn W 1964 *Phys. Rev.* B **136** 864–71
[18] Kresse G and Furthmüller J 1993 *Phys. Rev.* B **47** 558–61
[19] Kresse G and Furthmüller J 1996 *J. Comp. Mater. Sci.* **6** 15–50
[20] Perdew J P, Burke K and Ernzerhof M 1997 *Phys. Rev. Lett.* **78** 1396
[21] Monkhorst H J and Pack J D 1976 *Phys. Rev.* B **13** 5188–92
[22] Mujica A, Rubio A, Muñoz A and Needs R J 2003 *Rev. Mod. Phys.* **75** 863–912
[23] Parlinski K Computer code phonon (http://wolf.ifj.edu.pl/phonon/)
[24] Blanca-Romero A, Kowalski P M, Beridze G, Schlenz H and Bosbach D 2014 *J. Comp. Chem.* **35** 1339–46
[25] Cherniak D, Pyle J and Rakovan J 2004 *Am. Mineral.* **89** 1533–9
[26] Bauer J, Hirsch A, Bayarjargal L, Peters L, Roth G and Winkler B 2016 *Chem. Phys. Lett.* **654** 97–102
[27] Achary S N, Errandonea D, Muñoz A, Rodriguez-Hernadez P, Manjon F J, Krishna P S R, Patwe S J, Grover V and Tyagi A K 2013 *Dalton Trans.* **42** 14999–5015
[28] Syassen K 2008 *High Pressure Res.* **28** 75–126
[29] Mao H K, Xu J and Bell P M 1986 *J. Geophys. Res.* **91** 4673–6
[30] Errandonea D 2015 *Cryst. Res. Technol.* **50** 729–36
[31] Chai M and Brown J M 1996 *Geophys. Res. Lett.* **23** 3539–42
[32] Neupane M R, Garrett G A, Rudin S and Andzelm J W 2016 *J. Phys.: Condens. Matter* **28** 205501
[33] Adelstein N, Mun B S, Ray H L, Ross P N Jr, Neaton B and De Jonghe L C 2011 *Phys. Rev.* B **83** 205104
[34] Horchani-Naifer K and Ferid M 2009 *Inorg. Chim. Acta* **362** 1793–6
[35] Errandonea D, Muñoz A and Gonzalez-Platas J 2014 *J. Appl. Phys.* **115** 216101
[36] Bandiello E, Errandonea D, Martinez-Garcia D, Santamaria-Perez D and Manjon F J 2012 *Phys. Rev.* B **85** 024108
[37] Angel R J 2000 *Rev. Mineral. Geochem.* **41** 35–60
[38] Errandonea D, Muñoz A, Rodríguez-Hernández P, Proctor J E, Sapiña F and Bettinelli M 2015 *Inorg. Chem.* **54** 7524–35
[39] Lipinska-Kalita K E, Kalita P E, Hemmers O A and Hartmann T 2008 *Phys. Rev.* B **77** 094123
[40] Pereira A L J *et al* 2013 *J. Phys.: Condens. Matter* **25** 475402
[41] Errandonea D *et al* 2010 *Phys. Rev.* B **82** 174105
[42] Errandonea D, Ruiz-Fuertes J, Sans J A, Santamaría-Perez D, Gomis O, Gómez A and Sapiña F 2012 *Phys. Rev.* B **85** 144103
[43] Recio J M, Franco R, Martín Pendás A, Blanco M A, Pueyo L and Pandey R 2001 *Phys. Rev.* B **63** 184101
[44] Momma K and Izumi F 2011 *J. Appl. Crystallogr.* **44** 1272–6
[45] Knight K S 2010 *Phys. Chem. Miner.* **37** 529–33
[46] Landau L D and Lifshitz E M 1970 *Theory of Elasticity* (New York: Pergamon)
[47] Angel R J www.rossangel.com/text_strain.htm
[48] Nakamoto K 1986 *Infrared and Raman Spectra of Inorganic and Coordination Compounds* (New York: Wiley)
[49] Dawson P, Hargreave M M and Wilkinson G R 1971 *J. Phys.* C **4** 240–56
[50] Begun G M, Beall G W, Boatner L A and Gregor W J 1981 *J. Raman Spect.* **11** 273–8
[51] Silva E N, Ayala A P, Guedes I, Paschoal C W A, Moreira R L, Loong C K and Boatner L 2006 *Opt. Mater.* **29** 224–30
[52] Panchal V, López-Moreno S, Santamaría-Pérez D, Errandonea D, Manjón F J, Rodríguez-Hernández P, Muñoz A, Achary S N and Tyagi A K 2011 *Phys. Rev.* B **84** 024111
[53] Panchal V, Errandonea D, Manjón F J, Muñoz A, Rodríguez-Hernández P, Achary S N and Tyagi A K 2016 *J. Phys. Chem. Solids* **100** 126–33
[54] Canepa P, Hanson R M, Ugliengo P and Alfredsson M 2011 *J. Appl. Cryst.* **44** 225–9
[55] Hofmeister A M and Mao H-K 2002 *Proc. Natl Acad. Sci. USA* **99** 559–64
[56] Garg A B *et al* 2017 *Inorg. Chem.* **56** 5420–30
[57] Saviot L *et al* 2014 *J. Phys. Chem.* C **118** 10495–501
[58] Ruiz-Fuertes J *et al* 2001 *Phys. Rev.* B **83** 214112
[59] Gleissner J *et al* 2016 *Phys. Rev.* B **94** 134108
[60] Errandonea D, Gracia L, Beltran A, Vegas A and Meng Y 2011 *Phys. Rev.* B **84** 064103
[61] Errandonea D, Pellicer-Porres J, Pujol M C, Carvajal J J and Aguiló M 2015 *J. Alloys Compd.* **638** 14–20
[62] Manjón F J, Rodríguez-Hernández P, Muñoz A, Romero A H, Errandonea D and Syassen K 2010 *Phys. Rev.* B **81** 075202